A new planet candidate detected in a dust gap of the disk around HD 163296 through localized kinematic signatures: an observational validation of the DISCMINER

Izquierdo, A.F.; Facchini, S.; Rosotti, G.P.; Dishoeck, E.F. van; Testi, L.

The Astrophysical Journal, 928:2 (19pp), 2022 March 20 https://doi.org/10.3847/1538-4357/ac474d

A New Planet Candidate Detected in a Dust Gap of the Disk around HD 163296 through Localized Kinematic Signatures: An Observational Validation of the DISCMINER

Andrés F. Izquierdo[1,2], Stefano Facchini[1], Giovanni P. Rosotti[2,3], Ewine F. van Dishoeck[2,4], and Leonardo Testi[1,5]
[1] European Southern Observatory, Karl-Schwarzschild-Str. 2, D-85748 Garching bei München, Germany; andres.izquierdo.c@gmail.com
[2] Leiden Observatory, Leiden University, P.O. Box 9513, NL-2300 RA Leiden, The Netherlands
[3] School of Physics and Astronomy, University of Leicester, Leicester LE1 7RH, UK
[4] Max-Planck-Institut für extraterrestrische Physik, Gießenbachstr. 1, D-85748 Garching bei München, Germany
[5] INAF—Osservatorio Astrofisico di Arcetri, Largo E. Fermi 5, I-50125 Firenze, Italy
Received 2021 June 15; revised 2021 November 11; accepted 2021 December 29; published 2022 March 22

Abstract

We report the robust detection of coherent, localized deviations from Keplerian rotation possibly associated with the presence of two giant planets embedded in the disk around HD 163296. The analysis is performed using the DISCMINER channel map modeling framework on ^{12}CO $J = 2$–1 DSHARP data. Not only orbital radius but also azimuth of the planets are retrieved by our technique. One of the candidate planets, detected at $R = 94 \pm 6$ au, $\phi = 50° \pm 3°$ (P94), is near the center of one of the gaps in dust continuum emission and is consistent with a planet mass of 1 $M_{\rm Jup}$. The other planet, located at $R = 261 \pm 4$ au, $\phi = 57° \pm 1°$ (P261), is in the region where a velocity kink was previously observed in ^{12}CO channel maps. Also, we provide a simultaneous description of the height and temperature of the upper and lower emitting surfaces of the disk and propose the line width as a solid observable to track gas substructure. Using azimuthally averaged line width profiles, we detect gas gaps at $R = 38$, 88, and 136 au, closely matching the location of their dust and kinematical counterparts. Furthermore, we observe strong azimuthal asymmetries in line widths around the gas gap at $R = 88$ au, possibly linked to turbulent motions driven by the P94 planet. Our results confirm that the DISCMINER is capable of finding localized, otherwise unseen velocity perturbations thanks to its robust statistical framework, but also that it is well suited for studies of the gas properties and vertical structure of protoplanetary disks.

Unified Astronomy Thesaurus concepts: Protoplanetary disks (1300); Planetary-disk interactions (2204); Exoplanet detection methods (489)

1. Introduction

Detecting planets in the early stages of formation is key to reconstructing the history and diversity of fully developed planetary systems, including our own. However, the dense and opaque environment where planets are assembled—protoplanetary disks—makes the direct observation of these bodies a challenging task. To date, PDS 70 is the only system in which forming planets have been convincingly detected by direct imaging (Keppler et al. 2018; Haffert et al. 2019). Nevertheless, our growing understanding of how young planets interact with the disk material has stimulated the development of novel, albeit less direct, detection techniques.

Embedded planets are expected to produce velocity disturbances observable in molecular line emission through the gaseous component of their hosting disk (Perez et al. 2015; Pérez et al. 2018). In fact, there has been an increasing number of ALMA observations reporting localized (Pinte et al. 2018b; Casassus & Pérez 2019; Pinte et al. 2019) and extended deviations from Keplerian rotation (Teague et al. 2018, 2019) attributed to the presence of planets, which have naturally inspired theoretical efforts on the characterization and detection of planet-driven perturbations (Disk Dynamics Collaboration et al. 2020; Bollati et al. 2021; Izquierdo et al. 2021; Rabago & Zhu 2021). In particular, the disk around HD 163296, a Herbig Ae star at 101.5 pc from Earth (Bailer-Jones et al. 2018), has become one of the most interesting laboratories for the study of planet–disk interactions. It displays strong indications of embedded planets such as gaps and rings in the dust and non-Keplerian deviations to the velocity field in the gas.

As reported by Isella et al. (2016, 2018) using Band 6 continuum data, the dust gaps of the HD 163296 disk are located at a radial distance of 10, 45, 86, and 141 au from the star (referred to as D10, D45, D86, D141), and the dust emission rings at 14, 67, 100, and 159 au (referred to as B14, B67, B100, B159). An additional dust gap appears at 270 au[6] (or D270) according to former observations in optical scattered light by Grady et al. (2000). One way to explain these gaps is by invoking multiple embedded planets with masses between ~0.1 and 4 $M_{\rm Jup}$ depending on the physical properties of the disk (Zhang et al. 2018). However, multiple gaps driven by spiral waves from a single planet (Bae et al. 2017) or induced by nonplanetary mechanisms should not be discarded (see, e.g., Andrews 2020, for a review).

Luckily, further constraints on the presence of planets have been possible thanks to recent kinematical analyses of the molecular gas in the disk. For instance, Pinte et al. (2018b) observed a localized velocity perturbation in ^{12}CO channel maps, also known as a "kink," consistent with the presence of a 2 $M_{\rm Jup}$ planet at an orbital distance of 260 au according to hydrodynamic simulations. From here on we refer to this kink as K260. In the same disk, Teague et al. (2018) detected azimuthally extended deviations from Keplerian rotation driven by radially localized pressure gradients typical of gas gaps

[6] Rescaled to the latest distance to the source.

Table 1
List of Attributes Considered for the DISCMINER Model of ^{12}CO $J = 2$–1 Intensity Channel Maps from the Disk around HD 163296, and the Corresponding Best-fit Parameters

Attribute	Prescription	Best-fit Parameters for ^{12}CO $J = 2$–1			
Inclination	i	$i = 45.^{\circ}71$	...	...	...
Position angle	PA	PA $= 312.^{\circ}35$	...	...	...
Systemic velocity	$\upsilon_{\rm sys}$	$\upsilon_{\rm sys} = 5.77$ km s^{-1}	...	...	...
Rotation velocity	$\upsilon_k = \sqrt{\frac{GM_\star}{r^3}}R$	$M_\star = 1.97\ M_\odot$	...	...	...
Upper surface	$z_U = z_0(R/D_0)^p - z_1(R/D_0)^q$	$z_0 = 29.78$ au	$p = 1.21$	$z_1 = 4.36$ au	$q = 1.98$
Lower surface	$z_L = z_0(R/D_0)^p - z_1(R/D_0)^q$	$z_0 = 19.91$ au	$p = 1.09$	$z_1 = 0.03$ au	$q = 4.18$
Peak intensity	$I_p = I_0(R/D_0)^p(z/D_0)^q$	$I_0 = 8.23$ Jy pix^{-1}	$p = -4.16$	$q = 3.68$	...
Line width	$L_w = L_{w0}(R/D_0)^p(z/D_0)^q$	$L_{w0} = 0.08$ km s^{-1}	$p = 0.86$	$q = -1.38$	...
Line slope	$L_s = L_{s0}(R/D_0)^p$	$L_{s0} = 1.85$	$p = 0.21$	...	...

Note. $D_0 = 100$ au is a normalization constant, z is the height above the disk midplane, R is the cylindrical radius, and r is the spherical radius. The (down-sampled) pixel size of the model is 15.83 au. PA is the position angle of the semimajor axis of the disk on the redshifted side.

(Kanagawa et al. 2015). By modeling the rotation curve of the system, the authors found a plausible scenario consisting of gas gaps carved by two Jupiter-mass planets orbiting at 83 and 137 au. Moreover, at the radial location of these gaps, Teague et al. (2019) would later report the discovery of meridional circulation of gas flowing from the disk surface toward the midplane, providing further evidence for the presence of strong depletions in the surface density of the disk. However, these large-scale fluctuations associated with gas gaps should ideally be accompanied by the study of azimuthally localized perturbations in the velocity field in order to reduce the ambiguity that exists between planetary and nonplanetary mechanisms to explain the origin of such substructures (see, e.g., Izquierdo et al. 2021; Rabago & Zhu 2021).

In this article, we apply the DISCMINER channel map fitting analysis and statistical framework presented in Izquierdo et al. (2021) to search for embedded planets in the disk around HD 163296 using DSHARP ^{12}CO $J = 2$–1 archival data. The technique detects two azimuthally localized velocity perturbations possibly driven by two giant planets: one at $R = 94$ au, $\phi = 50^{\circ}$, within the D86 dust gap, and another at $R = 261$ au, $\phi = 57^{\circ}$, potentially linked to the K260 velocity kink. Additionally, we use a best-fit model of the channel maps from the data to study the vertical structure of the disk, as well as the radial gradient of temperatures and line widths observed on the upper and lower emitting surfaces of ^{12}CO.

While this paper was under review, further data on the source were published by the MAPS collaboration (Öberg et al. 2021). We have repeated the analysis of this work on the new data without finding differences affecting our conclusions. We will show a detailed analysis of the new data in a future publication.

2. Line Intensity Model of the HD 163296 Disk

2.1. Data Set

In this work we use ^{12}CO $J = 2$–1 line observations of the disk around HD 163296 obtained by the DSHARP ALMA Large Program (Isella et al. 2016, 2018; Andrews et al. 2018). The synthesized beam of the data is $0.''104 \times 0.''095$, and the velocity channels are spaced by 0.32 km s^{-1}. The rms noise per channel is 0.84 mJy beam^{-1}. The data cube is available at https://almascience.eso.org/almadata/lp/DSHARP. Details on the calibration of the data and imaging process can be found in Andrews et al. (2018).

2.2. DISCMINER Model Setup

To model the line intensity and kinematics of the disk, we use the DISCMINER package introduced in Izquierdo et al. (2021, hereafter Paper I). The DISCMINER assumes parametric prescriptions for the peak intensity, line width, rotation velocity, and height of the emitting surfaces of the disk to produce intensity channel maps. It then invokes the EMCEE sampler (Foreman-Mackey et al. 2013) to find the model parameters that best reproduce the intensity of the input data cube. This approach guarantees that the physical and morphological attributes of the disk are modeled simultaneously, providing a comprehensive picture of the gas disk structure and kinematics.

The DISCMINER pieces the disk attributes together in a predefined kernel to generate model line profiles and channel maps. As in Paper I, we adopt a generalized bell kernel to shape the model intensity, I_m, as a function of the disk cylindrical coordinates (R, z) as follows:

$$I_m(R, z; \upsilon_{\rm ch}) = I_p\left(1 + \left|\frac{\upsilon_{\rm ch} - \upsilon_k^{\rm l.o.s}}{L_w}\right|^{2L_s}\right)^{-1}, \quad (1)$$

where I_p is the peak intensity, L_w is half the line width at half power (or just line width from now on), and L_s is the line slope. For simplicity, we parameterize these attributes as power laws of the disk cylindrical coordinates (R, z). On the other hand, $\upsilon_{\rm ch}$ is the channel velocity where the intensity is to be computed, and $\upsilon_k^{\rm l.o.s}$ is the Keplerian line-of-sight velocity. The vertical coordinate z is determined by the height of the upper and lower emission surfaces, which implies that each attribute (except the line slope) has two different representations. The height of each surface is parameterized independently using a combination of two radial power laws. The exact functional form of each attribute and the free parameters of the model are summarized in Table 1.

To merge the contribution of the upper and lower emitting surfaces into a single line profile, on each velocity channel and pixel we select the highest intensity between bell profiles computed for both surfaces independently. In terms of radiative transfer, this type of masking is more precise than adding up

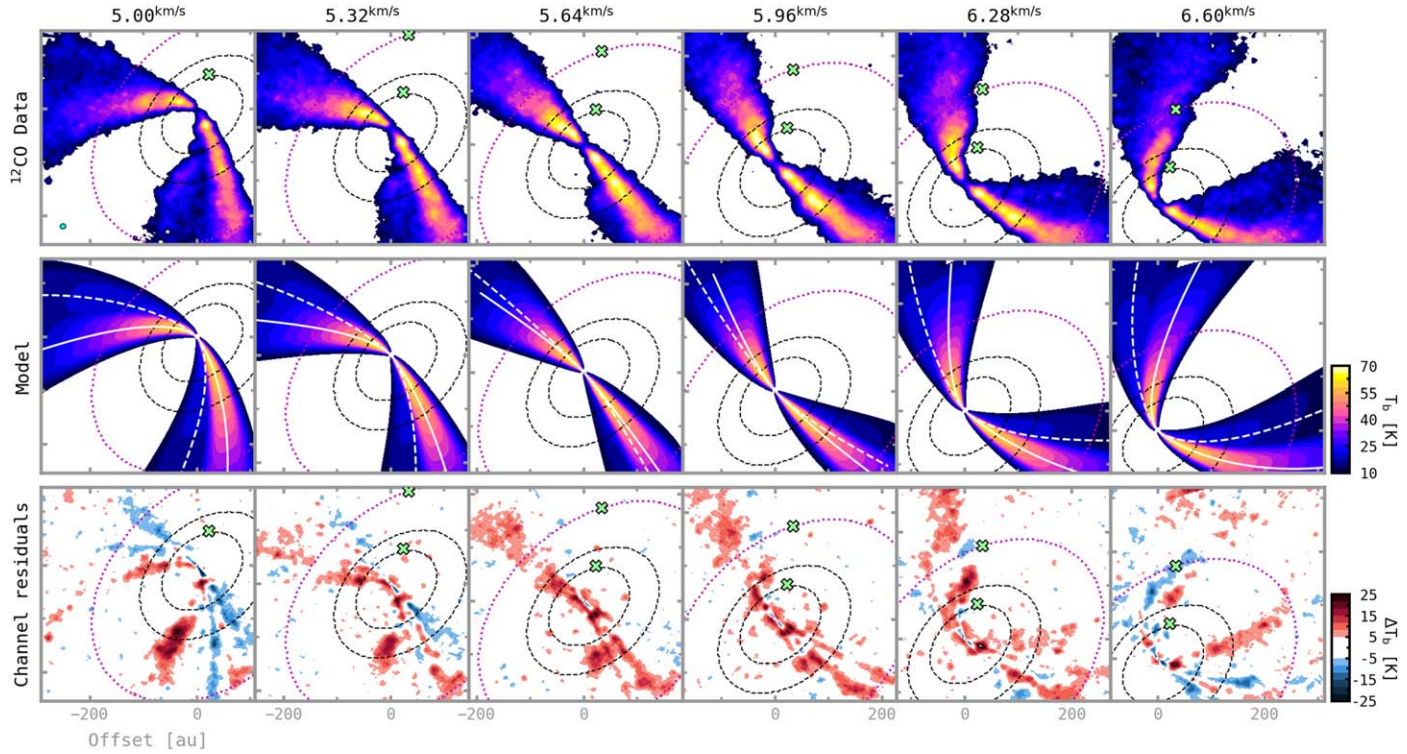

Figure 1. Selected channel maps from DSHARP ^{12}CO $J = 2$–1 data of the HD 163296 disk (top row), compared to those from the best-fit model found by the DISCMINER (middle row). Line-of-sight velocity contours from the model upper and lower surfaces of the disk are overlaid on the model channel maps as solid and dashed white lines, respectively. Also shown are residual brightness temperatures for each velocity channel (bottom row). For reference, the best-fit systemic velocity is $\upsilon_{\rm sys} = 5.77$ km s^{-1}. The synthesized beam of the observation is shown in the bottom left of the top left panel as a cyan ellipse. Velocity channels are spaced by 0.32 km s^{-1}. Residuals with magnitudes lower than the rms noise of the data were masked. Green crosses highlight the position of the localized velocity perturbations, P94 and P261, detected by our clustering algorithm in Section 3.4. Dashed black lines mark the projected location of the D86 and D141 dust gaps (Isella et al. 2018), while the dotted purple line shows the radial location of the K260 kink (Pinte et al. 2018b). From visual inspection, a localized kink-like feature near the P94 perturbation is observed in the $\upsilon_{\rm ch} = 5.96$ and 6.28 km s^{-1} channels. The K260 kink near the P261 perturbation is more extended, spanning from $\upsilon_{\rm ch} = 5.96$ to at least 6.92 km s^{-1} (see also Figure 7).

both intensity profiles directly. The reason is that in a real scenario the emission from the lower surface can only be distinguished when the upper surface becomes optically thin enough, which for ^{12}CO is mainly limited to the wings of the profile.[7]

It should be noted that the model attributes introduced here are merely descriptive and are not the result of detailed radiative transfer. Also, these are constrained to the upper and lower emitting surfaces of ^{12}CO $J = 2$–1, and therefore any extrapolation to other scale heights in the disk should be done with caution.

2.3. Parameter Search with EMCEE

We initialize the EMCEE sampler with a first guess of parameters according to previous measurements of the inclination, position angle, and stellar mass (Isella et al. 2018; Teague et al. 2019). The other initial parameters are guessed using the prototyping tool of the DISCMINER, which allows for a quick comparison of the morphology of model channel maps with respect to the data. The Markov Chain Monte Carlo (MCMC) search is performed with 256 walkers that evolve for 3000 steps for an initial burn-in stage. Next, to sample the posterior distributions and assess convergence of parameters, we run the same number of walkers for 10,000, 20,000, and 50,000 steps. We note that the variance and the median of parameter walkers remain almost unchanged after ∼10,000 steps. The best-fit parameters summarized in Table 1 are the median of the posterior distributions in the last 5000 steps of the 20,000 step run, thinned by half the autocorrelation times of the parameter chains in order to minimize the impact of nonindependent samples on the posterior statistics. In Figure 1, we compare selected channel maps from the data and the best-fit model obtained with these parameters.

On a side note, we observe that the best-fit stellar mass retrieved by our model is affected by the choice of the disk outer radius. For a disk radius of $R_d = 380$ au we find a stellar mass of $M_\star = 2.02\ M_\odot$, whereas for $R_d = 450$ au the stellar mass decreases to $M_\star = 1.97\ M_\odot$. This behavior is expected as the model tries to compensate for the sub-Keplerian rotation supported by steep pressure gradients at large disk radii (Dullemond et al. 2020). However, none of the results of this paper are affected by such a small variation in the stellar mass.

The noise of the data is taken into consideration for the parameter search as follows. At each pixel of the data, we compute the standard deviation of the residual intensities in line-free channels and take it as the weighting factor of the likelihood function to be maximized by the sampler (see Equation (1) of Paper I). To ensure that the noise of individual pixels is approximately independent from neighboring pixels, we down-sample the data and the model grid so that the pixels are separated by ∼1.5 beams between each other. Also, this enables us to safely consider the variance of the posterior

[7] Assuming that the sensitivity and the angular and spectral resolution of the observation are sufficient to resolve both emitting surfaces.

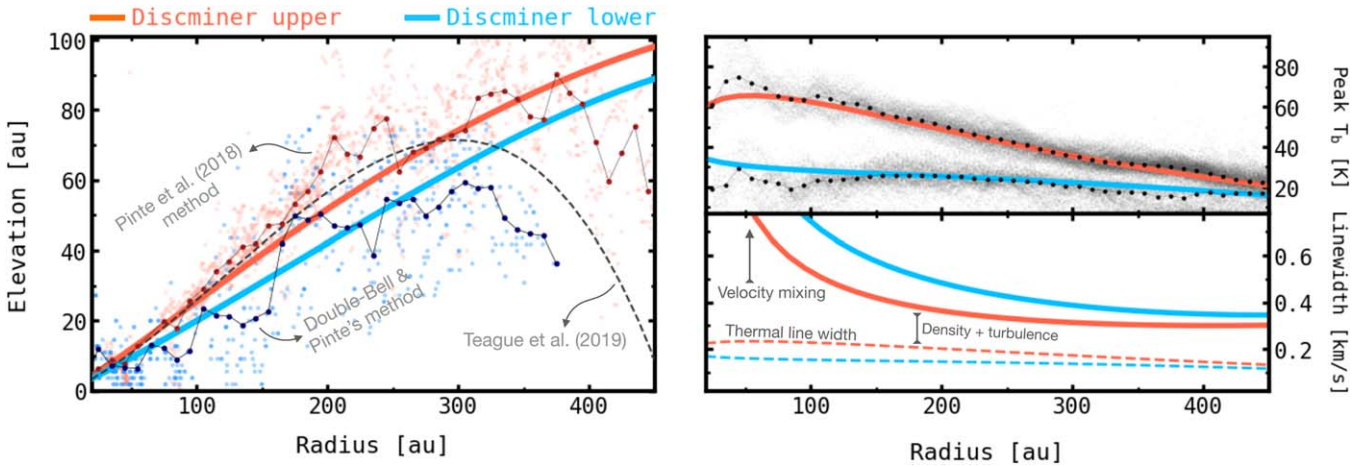

Figure 2. Best-fit attributes derived by the DISCMINER for the upper (solid orange) and lower (solid blue) emitting surfaces of ^{12}CO $J = 2$–1 in the disk of HD 163296. The functional forms of the model attributes and best-fit parameters are presented in Table 1. Left: height of the model emission surfaces. The background dots illustrate the height of the upper (orange) and lower (blue) surfaces derived independently with the method of Pinte et al. (2018a). See Section 3.1.1 for details on how to use the method on the lower surface alone. The connected circles mark the mean value of dots within 10 au (∼beam size) intervals. Also shown is the height reported by Teague et al. (2019). Top right: model peak brightness temperature, computed with the full Planck law. The background dots are the primary and secondary peaks, associated with emission from the upper and lower surface, respectively, as retrieved from double-Bell profiles fitted along the velocity axis of the data cube (see Section 3.1.1). Bottom right: model half line widths at half-maximum. The dashed lines indicate half the thermal broadening at half-maximum for ^{12}CO at the model temperatures of the top right panel. The difference between the thermal and the observed suprathermal line width is given by the contribution of density and turbulence to the optical depth of the line and by velocity mixing.

distribution of model parameters and their (anti)correlations to quantify uncertainties in observables derived from the model. Details on the analytic propagation of errors taking into account parameter correlations are presented in Appendix A.

3. Results

3.1. Physical Attributes of the ^{12}CO Disk

In this section, we discuss the form of the main physical attributes retrieved by the DISCMINER model of the ^{12}CO $J = 2$–1 emission from the disk around HD 163296. In Figure 2, peak brightness temperature, line width, and height of the upper and lower emitting surfaces are shown as a function of the radial location in the disk.

3.1.1. Emission Height

Our best-fit model indicates that the scale height of the upper surface of the disk is around $z/R \approx 0.26$, similar to the findings of Rosenfeld et al. (2013). This scale height is also in good agreement with the kinematical model of the upper surface reported by Teague et al. (2019), although they diverge substantially on the outskirts of the disk ($R > 300$ au). For further comparison, we also determined the height of the upper surface using the DISKSURF code (Teague et al. 2021b), which is an open-source implementation of the geometrical method introduced by Pinte et al. (2018a) for measuring the altitude of molecular line emission in disks. This independent experiment is better reproduced by the upper surface of the DISCMINER up to $R = 400$ au, although beyond that radius the three methods seem to differ. One of the reasons for this discrepancy may be the fact that the boundary to distinguish intensities from the upper and lower surfaces is diffuse toward the edge of the disk, and hence the extraction of the upper surface might be biased by the contribution of the lower counterpart. Nevertheless, our analysis of gas substructures and detection of planets takes place within $R < 300$ au, where the three measurements agree.

Unlike previous methods, the DISCMINER allows us to infer the height of the lower emitting surface too. Our model finds that the lower surface stands around $z/R \approx 0.2$ scale heights above the midplane of the disk. To validate this part of the modeling, we performed an empirical reconstruction of the lower surface intensity from the data and then estimated the altitude of its emission using once again the geometrical method of Pinte et al. (2018a). To do this, we first fit double-bell profiles along the velocity axis of the pixels of the data cube in an attempt to separate the upper and lower surface emission. Next, on each pixel we extract the bell profile with the smaller peak intensity of the two, which is normally associated with the lower surface contribution to the line intensity profile (see, e.g., Dullemond et al. 2020). Finally, we combine these secondary bell profiles from all pixels to generate channel maps of the lower surface alone. These channel maps can then be an input to the method of Pinte et al. (2018a) to determine the altitude of the lower surface emission, which is illustrated by the blue dots in the left panel of Figure 2. The DISCMINER height of the lower surface is consistent with this independent estimate, at least for $R < 300$ au, where our following analyses take place. Centroid velocities of the lower and upper surfaces obtained separately from this empirical reconstruction are presented in Figure 3.

3.1.2. Line Width and Brightness Temperature

Because of the high densities present in protoplanetary disks, the emission from abundant molecules such as ^{12}CO is optically thick almost everywhere. For a related reason, the level populations of these molecules can be safely considered in local thermodynamic equilibrium (Weaver et al. 2018). Both these facts imply that the peak intensity at the central channel of the line emission converges to the kinetic temperature of the gas, and it saturates over neighboring channels until the optical depth becomes low at the line wings. Thus, the extent of the plateau at the top of the line is highly influenced by the density of the species, and consequently so is the observed line width. Conversely, if the transition was optically thin, the line broadening

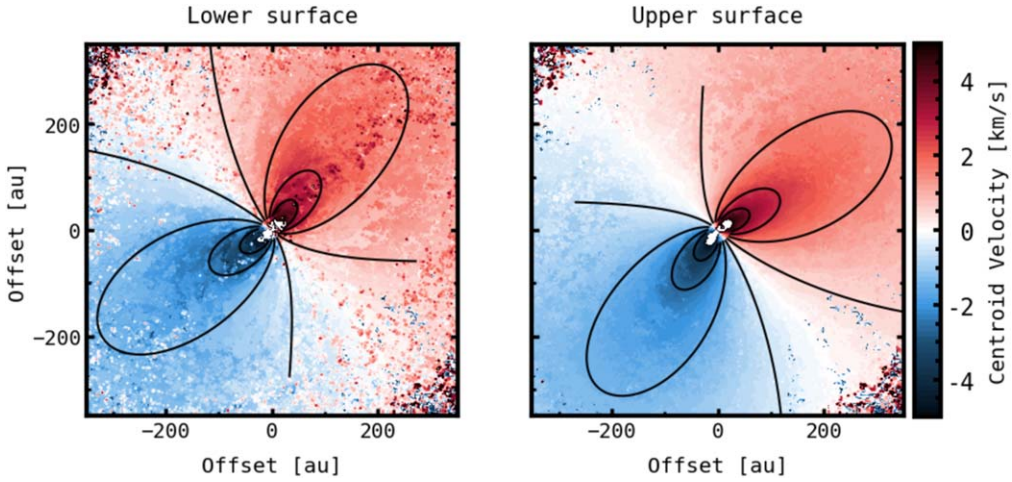

Figure 3. Empirical reconstruction of centroid velocities from the lower and upper emitting surfaces of the HD 163296 disk as observed in ^{12}CO $J = 2$–1, shifted to $v_{sys} = 5.77$ km s^{-1}. As explained in Section 3.1.1, this model-independent reconstruction consists of fitting double-Bell profiles to the data cube pixels along the velocity axis. For comparison, black contours are line-of-sight velocities from the DISCMINER best-fit model of the lower and upper surfaces of the disk, ranging from −3.5 to 3.5 km s^{-1} in steps of 1.0 km s^{-1}.

would be primarily dominated by thermal and turbulent motions (Hacar et al. 2016).

While the thermal broadening at half-maximum for ^{12}CO at 50 K is 0.21 km s^{-1}, the best-fit model line width at the same temperature (i.e., at $R = 140$ au, on the upper surface) can be as high as 0.43 km s^{-1}, and the contrast becomes even larger on the lower surface of the disk (0.15 vs. 0.60 km s^{-1}). This noticeable excess in line widths across the entire disk could be explained by strong turbulent motions in the gas. However, using observations of the HD 163296 disk with different molecules, Flaherty et al. (2017) obtained upper limits for turbulent broadening of only $\delta_{turb} < 0.06 c_s$, where c_s is the sound speed of the medium ($c_s = 0.50$ km s^{-1} at 50 K, assuming a unit mass for the medium of $\mu = 2.37$ u), which means that the suprathermal line widths should instead be dominated by the density of the species in most of the disk.[8] Such an opacity effect could explain why the retrieved line widths on the lower surface are generally higher than those on the upper surface despite the fact that the lower surface is considerably cooler. The width of the ^{12}CO line profile is thus an indirect window to the gas density, which we exploit in Section 3.3 to determine the location of gas gaps and analyze asymmetries in the gas substructure.

The peak brightness temperature of the model upper surface is consistent with the peak intensities measured directly from the data, which span a wide range of temperatures between ∼20 and 70 K (see also Isella et al. 2018). The peak brightness temperatures of the model lower surface oscillate between ∼20 and 30 K, which is compatible with temperatures where CO molecules are expected to freeze out onto dust grains (see, e.g., Miotello et al. 2014; Woitke et al. 2016). They also agree with previous radiative transfer models (Flaherty et al. 2015) and direct estimates (Dullemond et al. 2020), as well as with the secondary peak intensities retrieved independently by the double-bell fits introduced in Section 3.1.1.

3.2. Residual Maps

To extract observables and quantify line profile differences between the data cube and the smooth Keplerian model of the disk, we fit a Gaussian profile to each pixel of the data and the model cube.[9] The standard deviation, amplitude, and mean value of each Gaussian profile represent, respectively, the line width, peak intensity, and centroid velocity of the corresponding pixel. The Gaussian properties of the model line profiles are then subtracted from those of the data to produce line width, peak intensity, and centroid velocity residuals, as illustrated in Figure 4. Analogous to Paper I, the velocity residuals reported in this work are defined as the difference between the absolute value of data line centroids and the absolute value of model line centroids. Considering the absolute value before subtraction of velocities can be convenient for visualization because it makes residuals on the blueshifted side of the disk switch sign with respect to residuals computed from direct subtraction. This occurs in such a way that sub-Keplerian (super-Keplerian) perturbations in the azimuthal component of the velocity, as those expected around gas gaps, appear blue (red) in the residuals map. Differences between velocity residuals computed by direct subtraction and by subtraction of absolute values of line centroids are illustrated in Figure 12 in Appendix B.

It should be noted that our forward modeling of channel maps allows us to account for the effect of intensity variations on the retrieval of gas velocities from both model and data. For this reason, fitting Gaussians to full line profiles can be safely done. Note that this approach implies that the retrieved centroid velocities and line widths are the result of the combined contribution of the upper and lower surfaces to the intensity of the disk. For comparison, we explore another possibility using the quadratic fit method supported by the BETTERMOMENTS package (Teague & Foreman-Mackey 2018), which operates with intensity channels around line profile peaks to determine line-of-sight velocities, primarily representative of the upper surface of the disk (see Figure 4(d)).

Additionally, we use both kinds of velocity residuals, "upper +lower" and "upper-only," to find coherent filamentary

[8] At small radii, due to the finite angular and spectral resolutions, velocity mixing becomes the dominant source of line broadening.

[9] We fit Gaussian and not double-bell profiles because the data line centroids from the latter have high pixel-to-pixel variations, of the order of the channel width. This stage is not to be confused with the generation of model line profiles for the MCMC minimization of intensity differences discussed in Section 2.2.

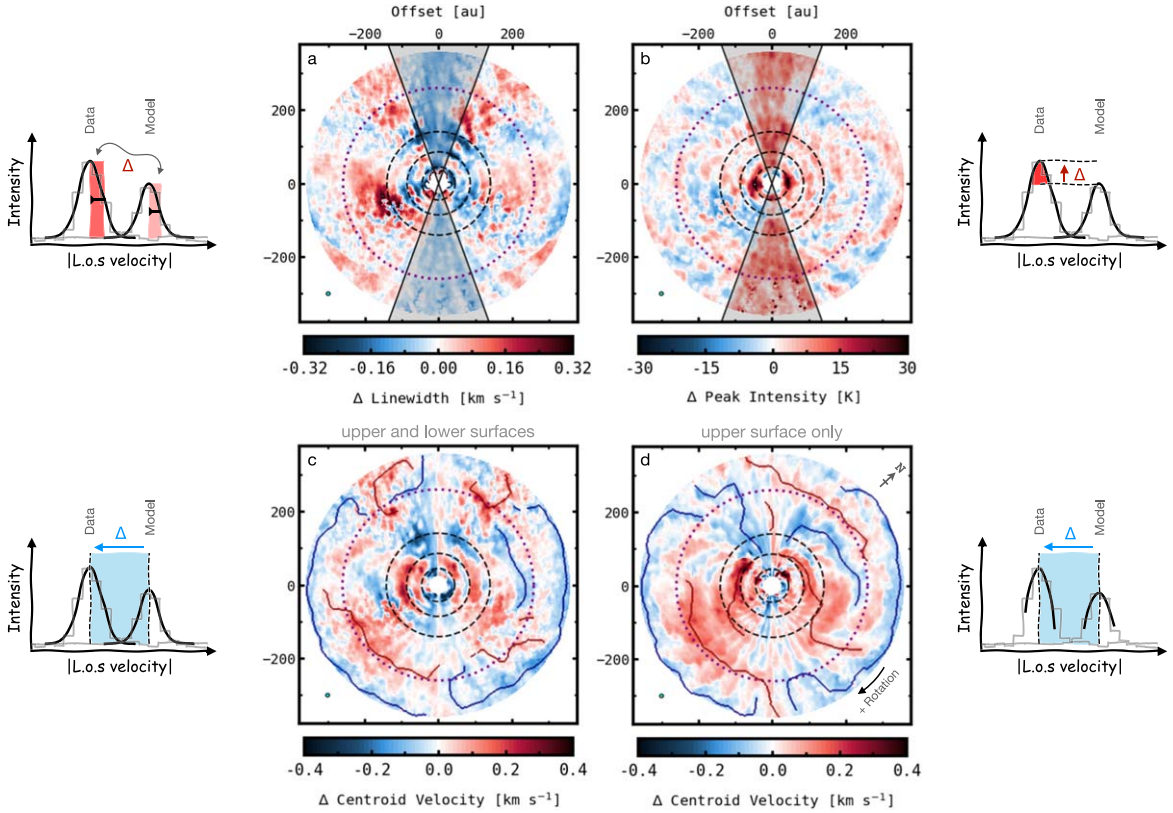

Figure 4. Deprojected residuals retrieved by (a–c) the DISCMINER and (d) BETTERMOMENTS by comparing ^{12}CO $J = 2$–1 observations of the disk around HD 163296 and best-fit line profiles found by the DISCMINER as described in Section 3.2. The cartoons next to each panel illustrate how the corresponding residuals are computed. The synthesized beam of the observation is shown in the lower left corner of all panels as a cyan ellipse. The beam is displayed as it is projected on the sky plane. For reference, the north axis of the sky plane and the rotation direction of the disk are marked in panel (d). Top row: (a) line width and (b) peak intensity residuals. The shadows indicate regions excluded from the analysis owing to systematic residuals possibly caused by velocity averaging in channels around the projected minor axis of the disk. Bottom row: velocity residuals obtained by subtracting the absolute value of data and model line centroids, which are (c) computed from full line profiles to account for the contribution of the upper and lower surfaces of the disk, or (d) measured around the peak of line profiles to which the upper surface contributes the most. Blue and red lines overlaid on velocity residuals are the spines of sub- and super-Keplerian filamentary structures found by FILFINDER. The dashed lines indicate the location of the D45, D86, and D141 dust continuum gaps registered by Isella et al. (2018). The outer dotted line marks the radial distance of the K260 kink reported by Pinte et al. (2018b).

structures with the FILFINDER package (Koch & Rosolowsky 2015). To start the search, we assume a smoothing size of 10 au, similar to the extent of the synthesized beam of the data, and a minimum size of 1500 pixels for a filament to be considered in the analysis. The red and blue lines overplotted in the bottom panels of Figure 4 are the medial axes of the filamentary structures found by the algorithm in our velocity residuals. In contrast, intensity and line width residuals do not exhibit elongated signatures as clearly. Nevertheless, in Section 3.3 we show that all three types of residuals provide remarkable clues about the gas substructure in the disk.

On the other hand, velocity residuals can also be used to hunt for candidate embedded planets. As demonstrated in Paper I, the presence of a planet is closely related to spatially localized velocity perturbations in the gas disk, whose magnitude and location should be retrievable as long as the resolution and signal-to-noise ratio of the data allow it.

In what remains, we focus our analysis on these three types of residuals to track gas substructure and to search for localized velocity perturbations possibly associated with the presence of young planets in the disk of HD 163296.

3.3. Gas Gaps

As discussed in Section 3.1.2, the line broadening of highly optically thick tracers is dominated by the species density, which in other words means that only a fraction of the line width originates from (non)thermal motions (Hacar et al. 2016). Therefore, ^{12}CO-depleted regions in disks are expected to drive prominent line width minima as illustrated in Paper I for a planet-carved gap. Line centroids are also sensitive to the presence of gaps owing to the fact that any gas substructure triggers local pressure forces that induce deviations from Keplerian rotation that follow the geometry of the pressure gradient. In the gas gap scenario, one can expect axisymmetric velocity perturbations with a positive radial gradient enclosed within the edges of the gap (Kanagawa et al. 2015; Teague et al. 2018). To exploit this background knowledge and search for gas gaps in the disk of HD 163296, we compute azimuthally averaged profiles of line width, peak intensity, and velocity residuals as displayed in Figure 5. This is done separately for the red- and blueshifted halves of the disk to highlight large-scale azimuthal asymmetries.

3.3.1. Azimuthally Averaged Residuals

From the average line width and velocity residual profiles there are clear indications of gas gaps near the D45, D86, and D141 dust gaps. Line width residuals exhibit local minima at $R = 38$, 88, and 136 au, closely coexisting with positive velocity gradients, and in good agreement with the location of gas gaps proposed by the radiative transfer modeling of

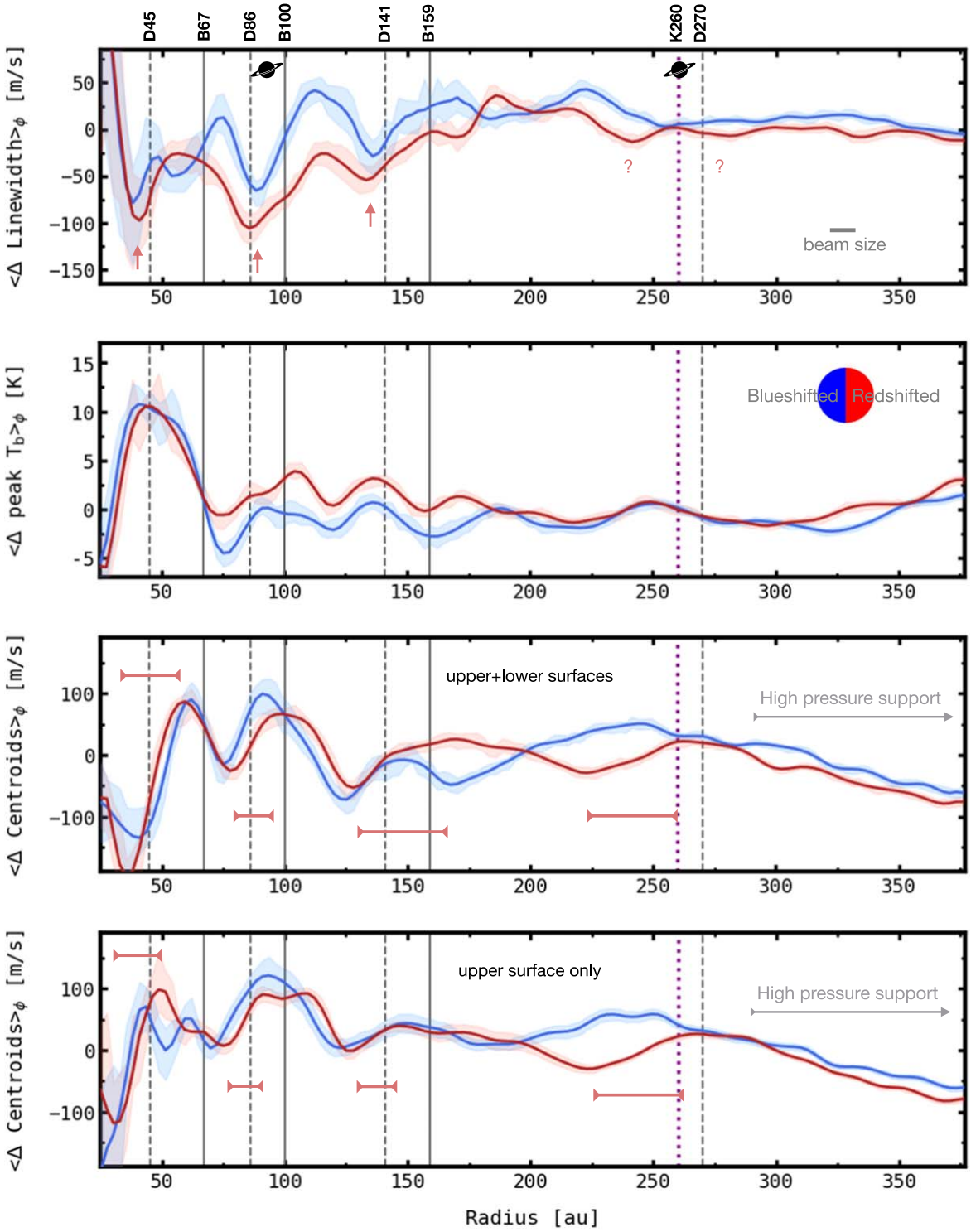

Figure 5. Azimuthally averaged line width, peak intensity, and centroid velocity residuals extracted from the blue- and redshifted halves of the disk, computed within $\pm 70^{\circ}$ azimuths to avoid systematic residuals near the disk minor axis (see Figure 4, top row). The radial location of dust gaps, dust rings, and the K260 kink is marked by the dashed, solid, and dotted lines, respectively. In the top panel is also shown the radial location of the two planet detections reported in Section 3.4. The shaded regions represent one standard deviation from the mean value, divided by the square root of the number of independent beams along each projected annulus. Gas gaps on the redshifted side of the disk are indicated by arrows and brackets; arrows mark local line width minima near dust gaps, while brackets enclose positive velocity gradients indicative of localized variations in the gas pressure.

Isella et al. (2016) and Liu et al. (2018). Also, the positive velocity gradients observed in our average velocity residuals are consistent with rotation curves of the same disk reported in recent studies (Teague et al. 2018; Rosotti et al. 2020). We note additional evidence of gas substructure near the K260 kink and the D270 dust gap, although this time the line width trough is not as clear as the closest positive velocity gradient, centered around $R = 245$ au on the redshifted half of the disk for both types of centroid residuals.

On the other hand, the average peak brightness temperature displays several local minima that do not overlap with the line width minima, nor with dust gaps or rings. Instead, some local

maxima seem to colocate with line width and dust gaps (D45,[10] D141), but there are multiple exceptions. Thus, looking at line width fluctuations in optically thick tracers appears to be a more reliable alternative to probing gas substructure. The reason is presumably that the line width is measured over the full line profile, so it can trace the systematic effect that the varying optical depth spawns over different velocity channels, while the peak intensity is measured on a single channel, making it more subject to local thermodynamic fluctuations and noise. Moreover, this means that the way in which gas gap attributes are retrieved could strongly impact the interpretation of hydrodynamic properties of disks and, more specifically, the inference of planet masses from radiative transfer models of gaps.

3.3.2. Nonaxisymmetric Gas Substructure

Our separate analysis of both halves of the disk allows us to comment on asymmetries present in the gas distribution and kinematics. Asymmetries in the gas velocities are subtle throughout most of the disk, but near the location of the K260 kink there is a significant radial shift of about ∼50 au between the peak of positive velocity gradients on each half of the disk. This is possibly an effect of nonaxisymmetric spiral-like perturbations (see Figure 4, bottom row), potentially linked to the hydrodynamic interaction of the disk and the massive planet detected by Pinte et al. (2018b) at $R = 260$ au, on the redshifted side. Another substantial asymmetry in average gas velocities is observed between 140 and 200 au. However, this feature appears on the "upper+lower" centroid residuals only, suggesting that instead of an actual asymmetry in the velocity field it could be related to contamination of the lower surface emission by dust absorption in the midplane of the disk (see Isella et al. 2018).

Unsurprisingly, there are asymmetries in the azimuthally averaged line width and intensity profiles too. Line widths are systematically lower on the redshifted part of the disk, between about B67 and B159, while peak intensities are slightly higher than those on the blueshifted side, in the same radial section. This finding reveals azimuthal fluctuations in the density and temperature of the disk: the blueshifted side of the disk is denser and cooler than the redshifted half. A plausible origin of these asymmetries may be the presence of massive planets, which are capable of producing vertical and turbulent motions that induce azimuthal gradients of velocity dispersion, density, and temperature around their orbit (Dong et al. 2019). The spatial coincidence of these features with the D86 and D141 gaps is in agreement with such a scenario. In particular, the blueshifted side of the disk has a prominent line width excess of ∼50 m s^{-1} in the D86 gap, which is similar to the expected excess that a massive planet would trigger in and around its gap (see Figure 8 of Dong et al. 2019). In Section 3.4, we detect an azimuthally localized velocity perturbation near D86, which strengthens the idea of an embedded planet at this location. Future studies of optically thin isotopologues could offer additional clues about candidate massive planets by characterizing line width and temperature asymmetries in the disk.

[10] However, the temperature peak at D45 is likely due to continuum subtraction and beam dilution in the inner 30 au of the disk (Teague et al. 2019). This behavior is captured by the model at the cost of underestimating temperatures around 50 au (see also Figure 2, top right).

3.4. Detection of Planets

We employ the statistical analysis developed in Paper I to search for localized planet-driven perturbations in the gas disk kinematics of HD 163296. More specifically, we use the so-called Variance Peak method of that framework to exploit the fact that peak deviations from Keplerian rotation are expected to be spatially clustered near planets.

The first step of the Variance Peak method consists of folding centroid velocity residuals (Figure 4, bottom row) along the projected minor axis of the disk to get rid of any axisymmetric feature driven by symmetric substructures such as gas gaps. In other words, we subtract line centroids on the blueshifted side of the disk from their mirror location on the redshifted half. Next, a radial scan is performed over the map of folded centroids to search for peak velocity residuals and to record their magnitude, azimuth, and radial location, as displayed in Figure 13 in Appendix B. With this information we run a K-means clustering algorithm (MacQueen 1967; Pedregosa et al. 2011) along the radial and azimuthal coordinates, independently, to look for localized velocity perturbations. The K-means algorithm subdivides the input residuals into a predefined number of clusters in such a way that the center of each cluster is the closest center to all the residuals in the cluster. Said differently, the input data are iteratively partitioned into Voronoi cells until convergence is reached, which in this case means until the sum of squared distances from the peak residuals to the center of their clusters is minimized. We refer the reader to Paper I, Section 4.4, for further details on the K-means algorithm applied to the analysis of velocity residuals. If a velocity perturbation is strong and coherent, the variance of its corresponding cluster of peak velocity residuals should be high and exceed the variance of the background clusters, as predicted in Paper I. If such an excess is higher than three times the dispersion of the background variances (i.e., $>3\sigma$), we claim that the velocity perturbation is localized and therefore possibly driven by a planet.

This is illustrated in Figure 6, where we present folded centroid velocity maps for one half of the deprojected disk and the localized perturbations detected by the Variance Peak method. The detection algorithm is applied on centroid velocities derived from the upper surface alone (top row) and from the combined contribution of the upper and lower surfaces (bottom row). For the latter case, we masked the inner part of the disk where there is obscuration of the lower surface emission due to dust absorption in the midplane (Isella et al. 2018). Nonuniform absorption features would trigger spurious velocity fluctuations that may bias the detection process.

3.4.1. P94 Perturbation

On the upper surface, our method finds a strong localized perturbation with an amplitude of $\delta\upsilon = 0.41$ km s^{-1}, centered at $R = 94 \pm 6$ au, $\phi = 50° \pm 3°$ (hereafter P94)[11] in the disk frame of reference. This perturbation is in good agreement with the presence of a planet previously hypothesized as the main driver of the D86 dust gap observed in continuum (Isella et al. 2018),

[11] Because of the folding procedure applied to the velocity residuals, the azimuth of the detected perturbation is degenerate with respect to the other half of the disk. That is, the same perturbation is found, with opposite sign, at $\phi = 180° - 50° = 123°$, near a candidate kink reported by Pinte et al. (2020) in the D86 gap. Nevertheless, since the localized perturbation has a "Doppler flip" morphology, we favor the detection at $\phi = 50°$, where the super-Keplerian part of it is exterior to the orbit of the planet and the sub-Keplerian part is interior. This is expected so long as the observed perturbation is not strongly dominated by radial velocity fluctuations, which is true for massive planets at azimuths between $\phi = 0°$ and $\phi = 70°$, as illustrated in Figure 5 of Paper I.

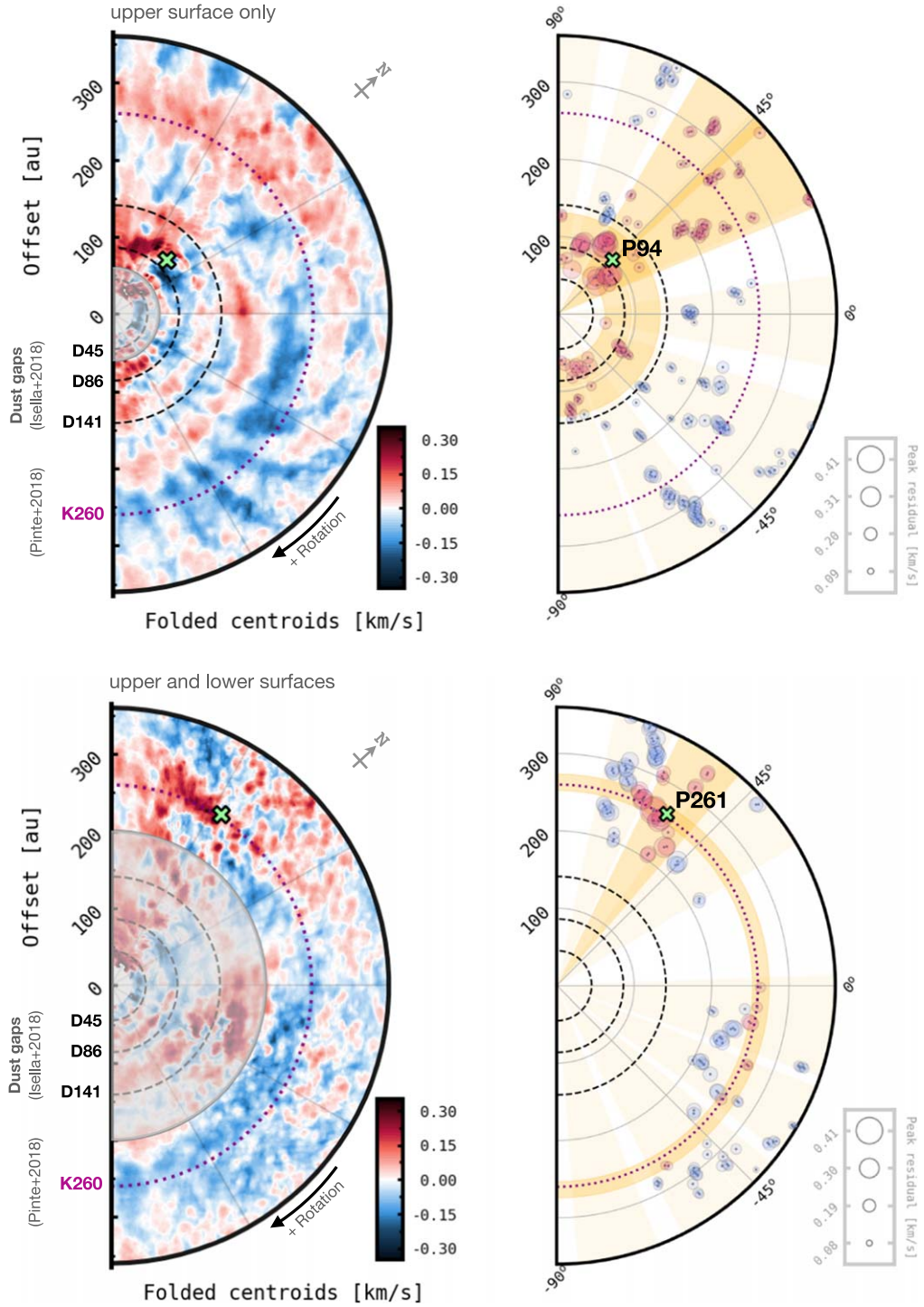

Figure 6. Folded velocity residuals (left column) and detected clusters of peak velocities (right) using seven radial and eight azimuthal clusters. The centroid velocities are measured either around the peak of the line profiles, namely, on the upper surface of the disk (top row), or using full line profiles, that is, considering the combined contribution of the upper and lower surfaces (bottom row). The green crosses mark the inferred position of the localized velocity perturbations detected by our clustering algorithm, P94 and P261, possibly driven by embedded planets. The gray regions in the left panels correspond to masked portions due to high velocity uncertainties (top; see Appendix A), or possible contamination of the lower surface by dust absorption in the midplane (bottom).

and of the corresponding gas gap inferred from pressure bumps in the rotation curve of the disk (Teague et al. 2018). The prominent line width asymmetries around the D86 gap further support the presence of this planet as discussed in Section 3.3. Also, P94 features a Doppler flip typical of spiral wakes generated by an embedded planet (Pérez et al. 2018; Casassus & Pérez 2019). We provide a rough estimate of the mass of this planet by rescaling the hydrodynamic simulations presented in Paper I, for a stellar mass of $2\,M_{\odot}$ and a planet at $R = 94$ au (see Figure 14 in Appendix B). Omitting radiative transfer effects, our simulations would predict that a $3\,M_{\rm Jup}$ planet can produce perturbations with an amplitude similar to that of P94. However, in Paper I we demonstrated that peak velocity fluctuations observed in folded velocity residuals can be amplified owing to radiative transfer and projection effects. In particular, in Figures 5 and 10 of that work we showed that at intermediate azimuths,

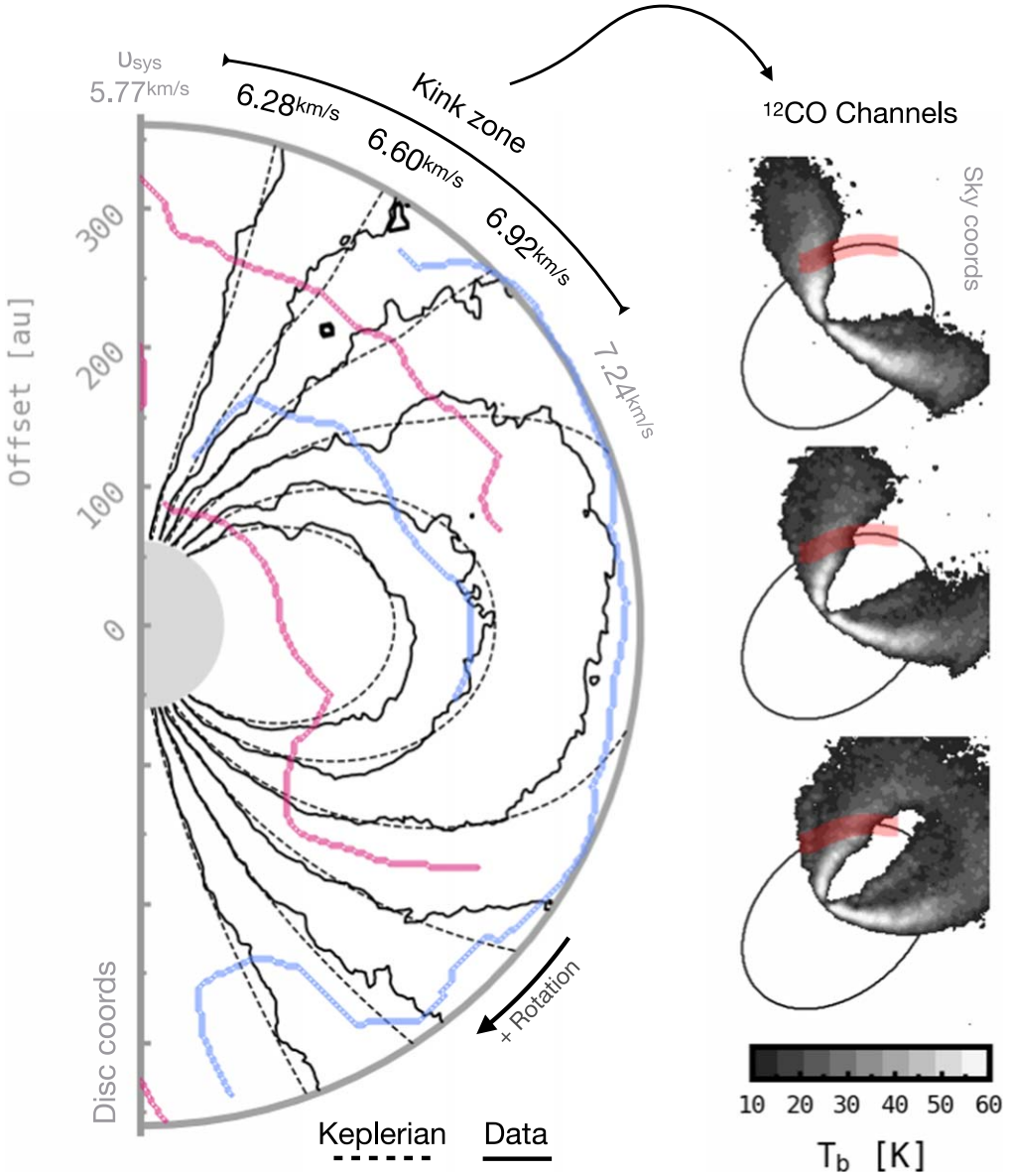

Figure 7. Illustrating isovelocity contours and deviations from Keplerian rotation related to the presence of coherent structures in the kinematics of HD 163296 as seen in ^{12}CO $J = 2$–1. The kink-like feature reported by Pinte et al. (2018b) is driven by the long red filament around $R = 260$ au (see also Figure 4(d)), spanning from 90° to 20° azimuths, which corresponds to a range of $\Delta v \approx 1.2$ km s^{-1} in velocity channels. Some of these channels are labelled at the top of the plot within the "Kink zone", and displayed in the right column panels in sky coordinates. This long kinematic substructure could be closely linked to the localised P261 perturbation and the associated planet candidate reported in Section 3.4.2.

between $\phi \approx 30°$ and $\phi \approx 60°$, an intrinsic perturbation of $\sim$0.25 km s^{-1} can become as large as $\sim$0.4 km s^{-1} when both effects are considered. Extending that result to this scenario, and by inspection of the left panel of Figure 14, a 1 $M_{\rm Jup}$ planet would be sufficient to explain the P94 perturbation, which is the same planet mass suggested by Teague et al. (2018) near the D86 gap. From Paper I, we also note that line width residuals as low as the observed $\Delta L_w \approx -0.1$ km s^{-1} at this radius are compatible with a deep gas gap carved by a 1 $M_{\rm Jup}$ planet too. Nevertheless, our mass estimate conflicts with the intermediate planet masses (0.1–0.3 $M_{\rm Jup}$) proposed by Zhang et al. (2018) at D86 based on hydrodynamic simulations of the dust gaps in the disk. This tension is expected because the dynamical properties of dust, which dictate how the dust grains interact with the gas in the disk, are still poorly constrained by observations. On the contrary, the use of kinematic measurements of planetary masses can help model the local properties of the dust with greater precision (Pinte et al. 2019). Nevertheless, we note that the accuracy of planet mass estimates from forward modeling of hydro simulations can still be systematically affected by a simplistic treatment of the gas thermodynamics (see, e.g., Bae et al. 2021).

3.4.2. P261 Perturbation

From the upper surface velocity residuals we do not find azimuthally localized perturbations linked to the K260 kink registered by Pinte et al. (2018b). Instead, we report that such a kink is actually driven by a long filamentary structure in the gas kinematics, spanning from $\sim$90° to 20° azimuths, and centered around $R \approx 260$ au. This is illustrated in Figure 7, where we compare isovelocity contours of the data against those of the DISCMINER model and highlight that the kink is present over

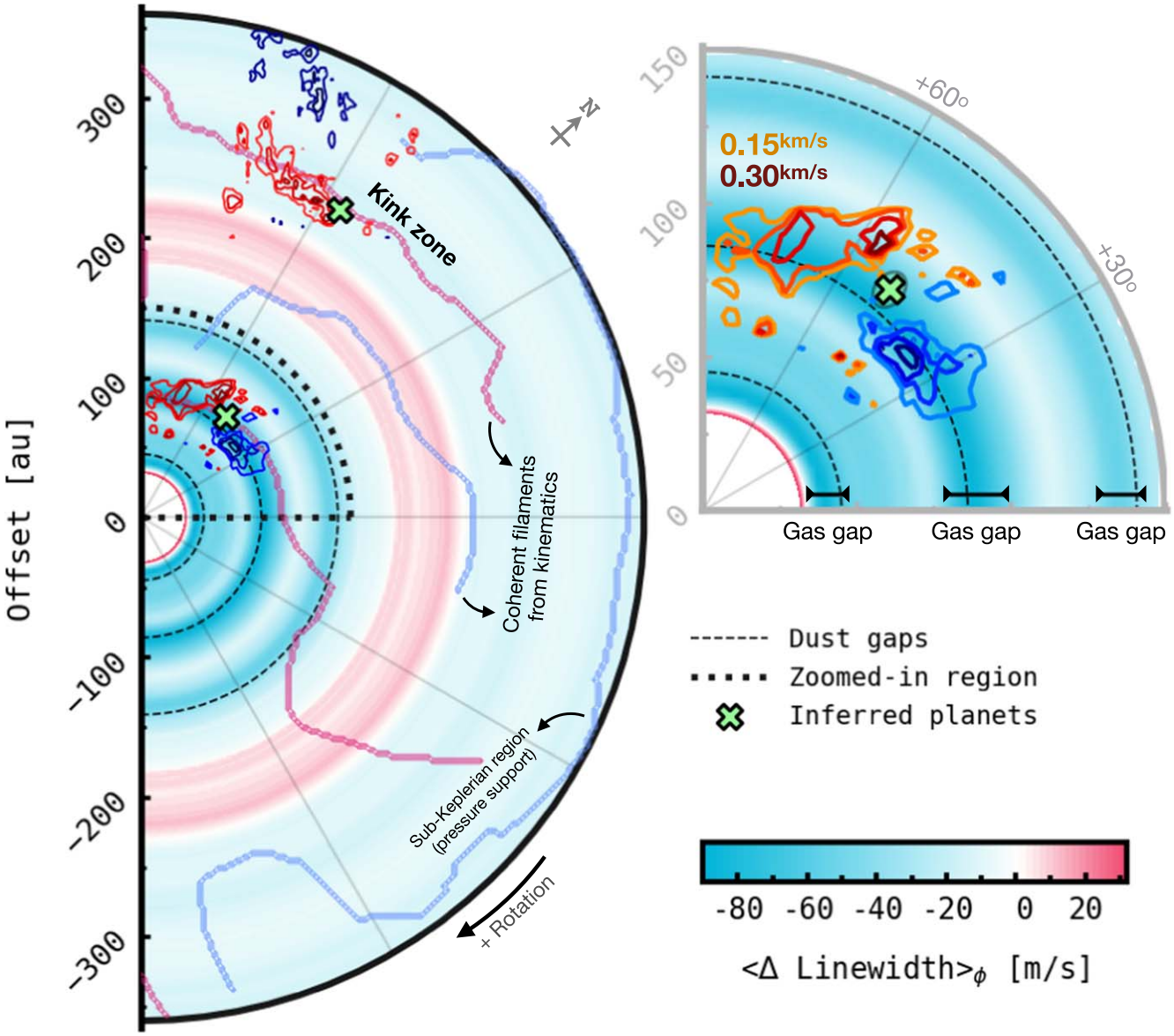

Figure 8. Summary of the main results of this work. The green crosses mark the inferred location of the P94 and P261 planets, and the blue–red contours, ranging from ±0.15 to ±0.30 in steps of 0.05 km s^{-1}, are nearby velocity residuals associated with the detections. The background colors are azimuthally averaged line width residuals to highlight the location of gas gaps. In light red and blue are overlaid the kinematic filamentary structures extracted from centroid velocity residuals on the upper surface of the disk. The quarter circle on the right is a zoom-in around the P94 perturbation, whose nearby velocity contours are this time colored according to their magnitude. The green ellipse centered on the P94 cross indicates the spatial error of the detection.

the channels that cross the $\delta\upsilon \approx 0.15$ km s^{-1} filament on the upper right corner of the deprojected disk. Conversely, there are a few other elongated deviations from Keplerian rotation that do not exhibit clear kinks to the eye because they are either weaker or stand at azimuths close to the main axes of the disk.

Nevertheless, when the combined contribution of the upper and lower surfaces is considered, a localized fluctuation of magnitude $\delta\upsilon = 0.40$ km s^{-1} appears at $R = 261 \pm 4$ au, $\phi = 57° \pm 1°$, in the region associated with the K260 kink. In Paper I, we have shown that planet-driven perturbations are sometimes best observed on the lower emitting surface owing to projection effects, especially for planets at intermediate azimuths in the near side of the disk, as in this case. Furthermore, it is also known that the magnitudes of the three-dimensional velocity perturbations around a planet change with scale height (see, e.g., Rabago & Zhu 2021), which could explain why the morphology and magnitude of the perturbation vary when the lower surface of the disk is taken into account. Both effects strengthen the idea that this localized perturbation (hereafter P261) should be caused by an embedded planet, which at the same time is likely to be the main driver of the long kinematic filament associated with the K260 kink.

3.4.3. Detection Significance of the Localized Perturbations

The significance of the P94 and P261 perturbations is above an acceptance threshold of 3σ with respect to the background velocity residuals. We note that both localized signatures are robustly detected regardless of the number of clusters considered for the K-means algorithm, which we tested using 6–10 clusters. The P94 detection yields an average significance of 19.4σ in radius and 7.5σ in azimuth, while the P261 detection has an average significance of 5.2σ in radius and 4.6σ in azimuth. Typical mean values of background cluster variances are between $(0.3–0.4) \times 10^{-3}$ km^2 s^{-2} and $(0.5–0.6) \times 10^{-3}$ km^2 s^{-2} for the

P94 and P261 analyses, respectively, while 1σ values are within $(0.1–0.2) \times 10^{-3}$ km^2 s^{-2} and $(0.3–0.4) \times 10^{-3}$ km^2 s^{-2}, where σ represents the standard deviation of background cluster variances. The reported orbital radius and azimuth of P94 and P261 is the mean value of the detected location weighted by the statistical significance of the measurement, while the reported uncertainty is the weighted standard deviation of the detected locations in all realizations.

3.4.4. Nondetections

Our algorithm does not detect any localized perturbation around the D141 gap. Assuming that this gap originates from a planet, our rescaled simulations suggest that it should be a low-mass planet of the order of 0.5 $M_{\rm Jup}$ or less, so that the planet-driven perturbations are blurred with the background $\delta\upsilon \approx 0.1$ km s^{-1} velocities (see Figure 14 in Appendix B, right panel). Furthermore, as demonstrated in Figure 6 of Paper I, average line width residuals of only $\Delta L_w \approx -0.05$ km s^{-1} such as those around D141 would be compatible with a gas gap opened by a low-mass planet ($<1\,M_{\rm Jup}$). On the other hand, as displayed in Figure 6, velocity fluctuations in the D45 gap can be as high as $\delta\upsilon \approx 0.45$ km s^{-1}, consistent with an embedded giant planet. However, the large azimuthal extent of these perturbations, spanning from $-30°$ to $+60°$ in the disk, prevents the method from detecting any localized signal there and affects the detection of features beyond. Moreover, D45 is inside the region where the errors in the observed velocities exceed 0.1 km s^{-1}. For these reasons we exclude the D45 gap from the detection analysis.

4. Conclusions

We employed the DISCMINER channel map modeling framework and statistical analysis introduced in Izquierdo et al. (2021) to search for localized velocity perturbations in the disk of HD 163296 using ^{12}CO $J = 2$–1 DSHARP data. Our study aims at retrieving not only radial distance but also azimuth of the localized perturbations, which is a natural step forward in the field. We report the robust detection of two coherent, localized fluctuations possibly driven by two giant planets at $R = 94 \pm 6$ au, $\phi = 50° \pm 3°$, and $R = 261 \pm 4$ au, $\phi = 57° \pm 1°$, labeled here as P94 and P261, respectively. The P261 perturbation is in the region of a kink-like feature previously observed by Pinte et al. (2018b) in intensity channel maps and attributed to an unseen 2 $M_{\rm Jup}$ planet. The P94 perturbation is consistent with the presence of a 1 $M_{\rm Jup}$ planet near the center of the D86 dust gap, which is in turn potentially linked to the radially localized pressure bump reported by Teague et al. (2018) at $R = 83$ au. The presence of this massive planet could also explain the nonaxisymmetric line widths retrieved by our analysis around the D86 gap.

Additionally, we use line profile properties to infer the location of gas gaps and nonaxisymmetric substructures in the disk. Based on line width residuals, we detect three gaps centered at $R = 38$, 88, and 136 au, compatible with prior radiative transfer models and kinematical measurements of radially localized pressure gradients. On the other hand, the height of the upper emitting surface retrieved by our model at $z/R \approx 0.26$ is in good agreement with previous estimates from geometrical and kinematical models. Simultaneously, we provide a model for the lower emitting surface of the disk, which stands at an altitude of $z/R \approx 0.2$ above the midplane and displays brightness temperatures near the CO freeze-out temperature. An illustrative diagram summarizing the main findings of this article is presented in Figure 8.

The authors would like to thank the anonymous referee for their constructive remarks and suggestions that allowed us to improve the robustness of the results and the overall quality of the manuscript. This work was partly supported by the Italian Ministero dell Istruzione, Università e Ricerca through the grant Progetti Premiali 2012—iALMA (CUP C52I13000140001), by the Deutsche Forschungs-gemeinschaft (DFG, German Research Foundation)—Ref. no. FOR 2634/1 TE 1024/1-1, and by the DFG cluster of excellence Origins (www.origins-cluster.de). This project has received funding from the European Union's Horizon 2020 research and innovation program under the Marie Sklodowska-Curie grant agreement No. 823823 (DUSTBUSTERS) and from the European Research Council (ERC) via the ERC Synergy Grant *ECOGAL* (grant 855130). S.F. acknowledges an ESO fellowship. G.R. acknowledges support from the Netherlands Organisation for Scientific Research (NWO, program No. 016.Veni.192.233) and from an STFC Ernest Rutherford Fellowship (grant No. ST/T003855/1).

Software: BETTERMOMENTS (Teague & Foreman-Mackey 2018), DISCMINER (Izquierdo et al. 2021), DISKSURF (Teague et al. 2021b), EMCEE (Foreman-Mackey et al. 2013), FILFINDER (Koch & Rosolowsky 2015), MATPLOTLIB (Hunter 2007), SCIKIT-LEARN (Pedregosa et al. 2011).

Appendix A
Analytic Propagation of Errors

To calculate uncertainties in the model attributes and in the derived residual maps, we use analytic formulae for the propagation of errors considering the variance of the posterior distributions of model parameters obtained with the EMCEE sampler in Section 2.3 and the variance of the measured line width, velocity, and peak intensity maps presented in Section 3.2.

The validity of this approach is subject to the assumption that the response of the mathematical model f, which transforms a set of input variables $\{X_0, X_1,\ldots,X_i,..,X_n\}$ with variances σ_i^2 into at least one output attribute Y with variance σ_y^2, is approximately linear within the variable variances. The DISCMINER system is a multi-input, multi-output transformation in the sense that it handles multiple input free parameters to model multiple output attributes, including peak intensity, line width, emission height, line slope, and rotation velocity, as prescribed in Table 1, as well as intensity channel maps following Equation (1), which depends on the aforementioned attributes.

A practical approximation of the variance σ_y^2 of the resulting distribution of the attribute $Y = f(X_0, X_1,\ldots,X_n)$ can be found by writing a first-order Taylor series expansion around the expected value of the input parameters $E[X_0]$, $E[X_1]$...,$E[X_n]$ and operating from the definition of variance, which gives

$$\sigma_y^2 = E[(Y - E[Y])^2] = \sum_i \frac{\partial f}{\partial X_i}^2 \sigma_i^2 + \sum_{ij}^{i\neq j} \frac{\partial f}{\partial X_i}\frac{\partial f}{\partial X_j}\sigma_i\sigma_j\rho_{ij}, \tag{A1}$$

where $\rho_{ij} \in [-1, 1]$ is the Pearson correlation coefficient between parameter pairs X_i, X_j. This analytic formulation has the advantage that the degree of (anti)correlation between

model parameters is accurately considered while keeping processing times short.[12] The posterior distributions of model parameters and their correlation coefficients are presented in Figures 9 and 11, respectively. We note strong (anti) correlations for several parameters, especially between peak intensity, line width, and emission height parameters. Rotation velocity, orientation, and line slope parameters are less dependent on one another.

To verify that the analytical variance of model attributes is a good representation of the statistical uncertainties of the MCMC search, we performed a comparison between 3σ regions predicted by Equation (A1) and the model attributes computed with random parameter samples selected from the posterior distributions. In Figure 10, we show that both regions are closely equivalent, suggesting that (a) the model response is far from nonlinear within at least a few sigma intervals and (b) the correlations between parameters are reasonably well captured by our analytical treatment.

Once the uncertainties in the model attributes have been computed, they are added to the measurement error of line profile properties to obtain the uncertainty of each model observable, assuming the worst-case scenario, which is full correlation between both variables. For instance, the uncertainty of the model centroid velocity is simply the sum of the MCMC uncertainty of the rotation velocity on the upper and lower surfaces, and the error in the observed velocity computed through the Gaussian fit, $\sigma_{v_{c[\mathrm{model}]}} = \sigma_{v_{[\mathrm{lower}]}} + \sigma_{v_{[\mathrm{upper}]}} + \sigma_{v_{\mathrm{obs}}}$, or through the quadratic fit from BETTERMOMENTS,$\sigma_{v_{c[\mathrm{model}]}} = \sigma_{v_{[\mathrm{upper}]}} + \sigma_{v_{\mathrm{obs}}}$.

Finally, the uncertainty in the residual maps is calculated assuming that the measurement errors on the model and the data are independent between each other. Taking the previous example, the uncertainty in centroid velocity residuals is thus given by $\sigma_{\Delta v_c} = \sqrt{\sigma^2_{v_{c[\mathrm{model}]}} + \sigma^2_{v_{c[\mathrm{data}]}}}$. It is followed equivalently for line width and peak intensity residuals. In Figure 11, right column, we present the uncertainties derived for the four different residual maps introduced in Figure 4. We note that the errors in residual maps are dominated by the uncertainties of the data. For instance, the errors of centroid velocities in the data are typically twice as large as the errors of model centroid velocities, of which less than 5% correspond to statistical uncertainties from the MCMC search. The various components making up the error in centroid velocity residuals are illustrated in the bottom row of Figure 10.

The most visible feature in the error maps of residuals is that those derived from Gaussian fits have a cross pattern following diagonal axes of the disk. This is due to the influence of the lower surface on the line profile that is increasingly prominent as one moves away from the main projected axes of the disk, and so it is the uncertainty of the Gaussian fit properties. It follows reciprocally that the quadratic fit method, which is mainly narrowed to the upper surface of the disk, yields errors that are relatively uniform in azimuth. Nevertheless, errors in centroid velocities measured with Gaussian fits are generally smaller than those from the quadratic fits, for which channelization effects are already evident. This is why for the analysis of localized velocity perturbations on the upper surface of the disk, presented in Section 3.4, we mask the inner 60 au, where the residual errors are larger than 0.1 km s^{-1} on average.

[12] We note that even though a direct sampling of the posterior distributions would be more accurate at deriving uncertainties in the residual maps, it does not compensate for the immense computational cost it implies to measure, store, and analyze line profile properties from several thousands of model cubes simultaneously.

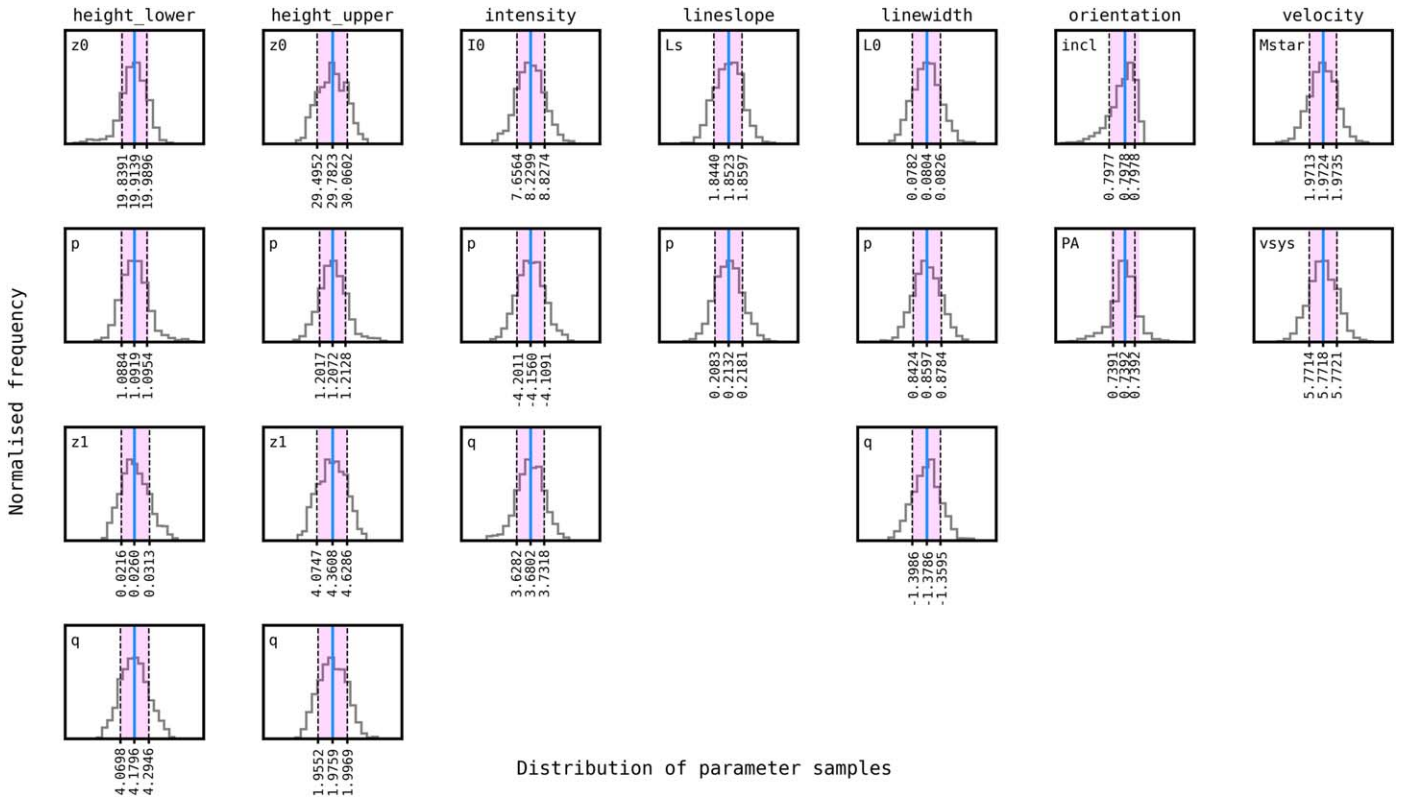

Figure 9. Posterior distributions of DISCMINER model parameters from 256 walkers in the last 5000 steps of a 20,000-step run performed by EMCEE, thinned by half the autocorrelation times of the parameter chains in order to minimize the impact of nonindependent samples on the posterior statistics. This run was preceded by a burn-in stage of 3000 steps as specified in Section 2.3. The blue lines indicate the median of parameters (summarized in Table 1), which are used to generate the best-fit model channel maps. The shades in magenta represent ± 1 standard deviations, whereas dashed lines are 15.9 and 84.1 percentiles. The small differences between 1σ regions and percentiles suggest that the posterior distributions are nearly normal.

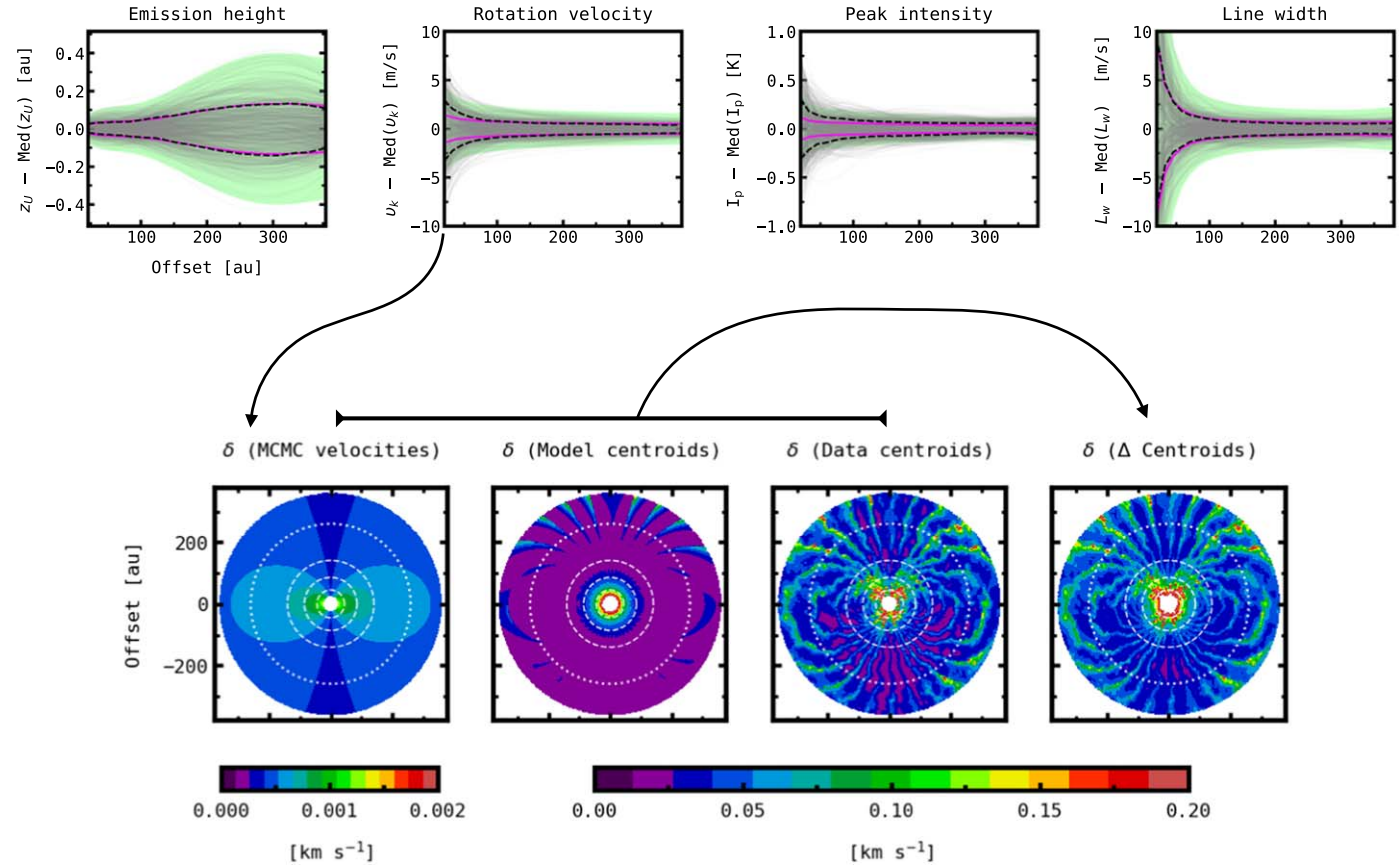

Figure 10. Top row: illustrating how statistical uncertainties of the MCMC search impact the distribution of model attributes. The gray lines are attributes computed for 1000 parameter samples selected randomly from the MCMC posterior distributions. The dashed black lines represent 15.9 and 84.1 percentiles. For comparison, the background shades in green and magenta lines are 3σ and 1σ uncertainties derived analytically using Equation (A1), which reproduce the dispersion of model attributes reasonably well. For a better visualization, the model attributes are referred to their median value. Uncertainties in the rotation velocity are projected on the sky plane and computed along $\phi = 0^{\circ}$ azimuth. Bottom row: deprojected uncertainties from the different components involved in the error propagation of centroid velocity residuals. Note that uncertainties in the measurement of data centroids are strongly dominant. The dashed lines indicate the location of the D45, D86, and D141 dust continuum gaps, and the dotted line marks the radial distance of the K260 kink.

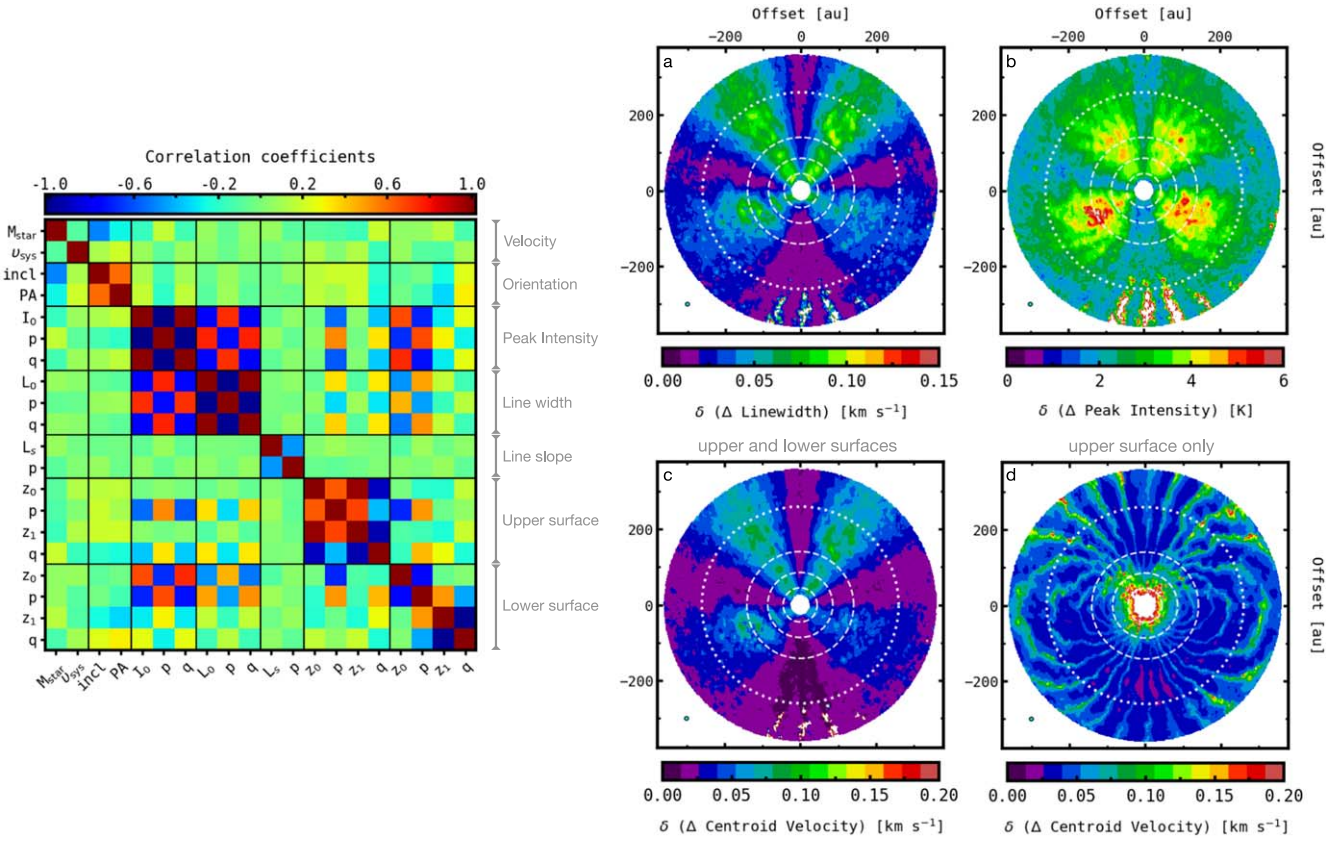

Figure 11. Left panel: Pearson correlation coefficients (ρ_{ij}) between model parameters. These coefficients are employed to calculate the contribution of crossed derivatives to the output variance of model attributes (see Equation (A1)). The parameters are grouped according to their corresponding attribute. Right panels: deprojected uncertainties of the residual maps presented in Figure 4, computed according to the analytical formulation of errors introduced in Appendix A. The dashed lines indicate the location of the D45, D86, and D141 dust continuum gaps, and the dotted line marks the radial distance of the K260 kink.

Appendix B
Supporting Figures

In this Appendix, we provide additional figures to illustrate details discussed in Section 3 on the gas kinematics and detection of planets in the disk of HD 163296. Figure 12 compares velocity residual maps computed with different subtraction methods. Figure 13 shows the observed location of peak velocity residuals as a function of azimuth and radius in the disk, which are employed to search for localized perturbations as explained in Section 3.4. Finally, Figure 14 presents the variation of peak velocity residuals as a function of planet mass and azimuth obtained from hydrodynamic simulations of planet-disk interactions.

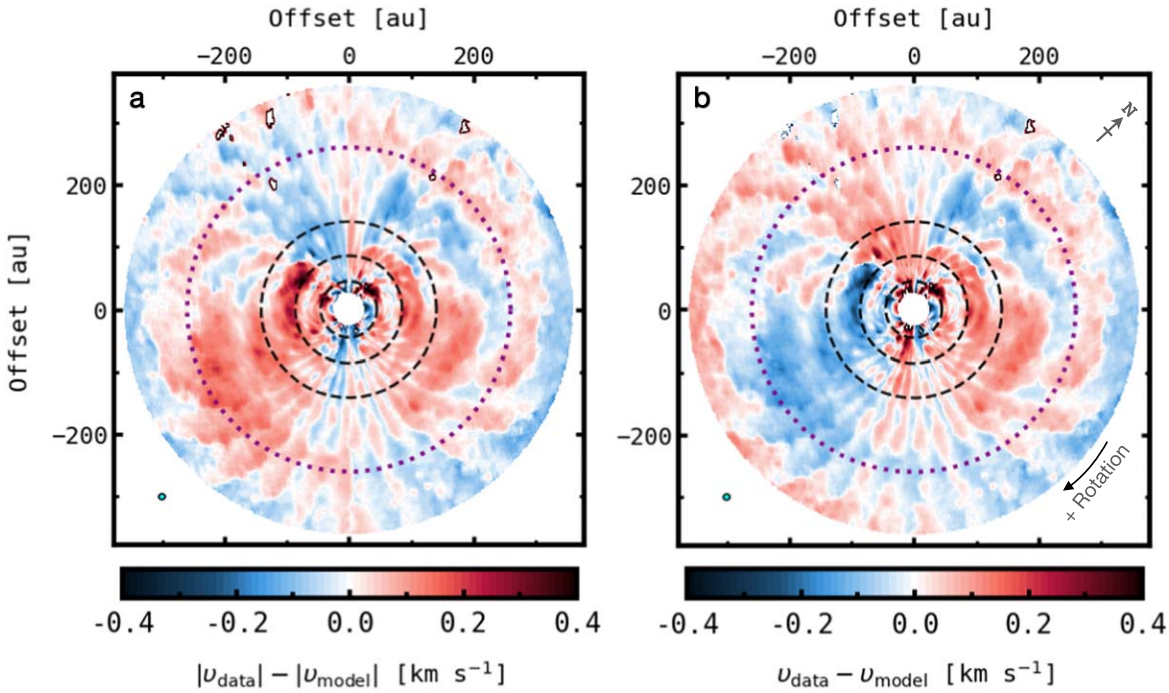

Figure 12. Comparison between velocity residuals obtained from different subtraction methods. In the left panel, the absolute value of data and model line centroids is taken before subtraction, while in the right panel a direct subtraction is performed. Considering the absolute value can be convenient for visualization because it makes residuals on the blueshifted side of the disk switch signs in such a way that sub-Keplerian (super-Keplerian) perturbations in the azimuthal component of the velocity, such as those expected around gas gaps, appear blue (red). The main signatures of velocity residuals in panel (b) are qualitatively similar to those found by Teague et al. (2021a). Local differences are due to the fact that (1) our model velocities account for the impact of spatial variations in intensity and (2) we do not consider any kernel to spatially smooth our residual maps. The dashed lines indicate the location of the D45, D86, and D141 dust continuum gaps registered by Isella et al. (2018). The outer dotted line marks the radial distance of the K260 kink reported by Pinte et al. (2018b).

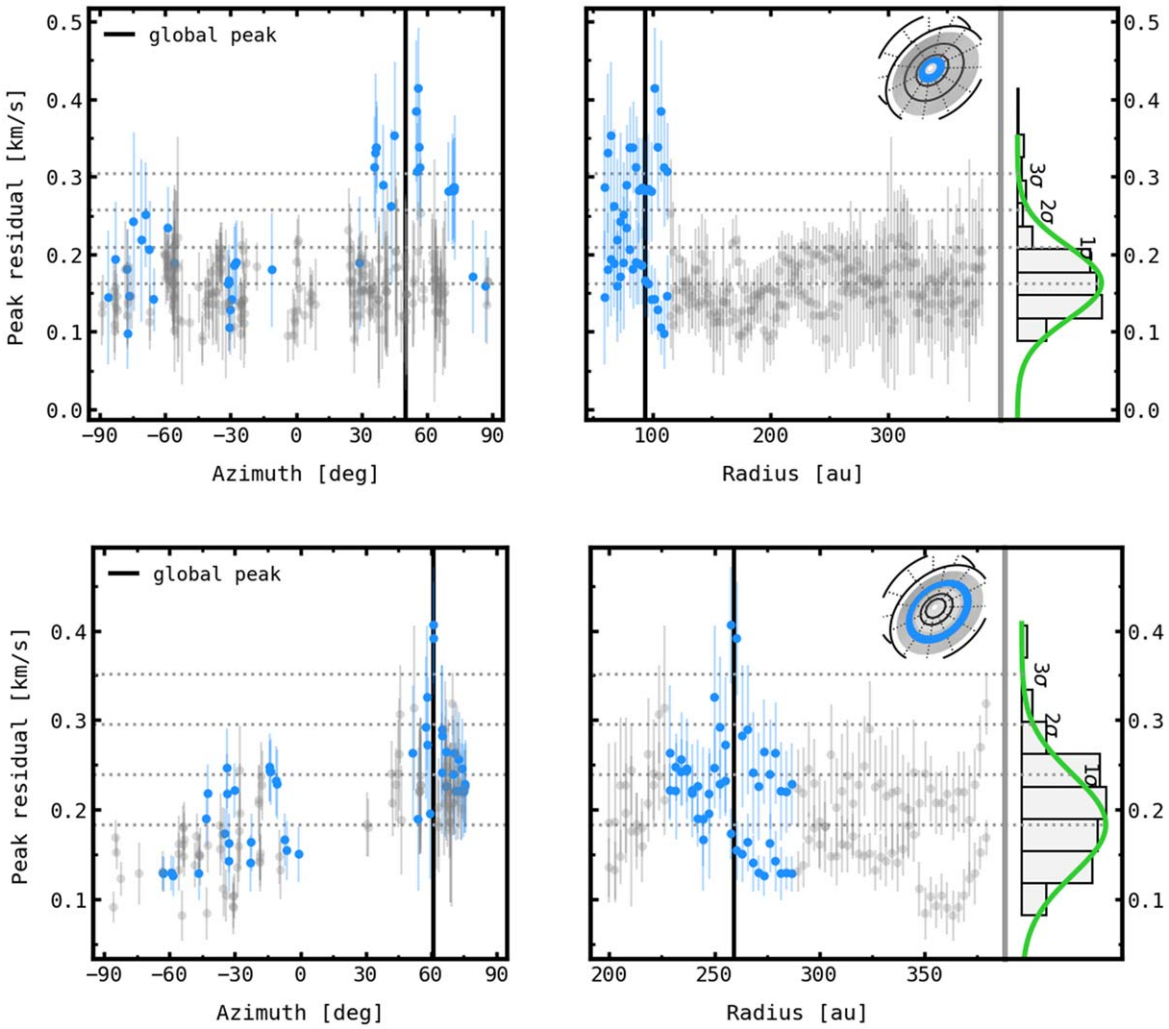

Figure 13. Location of peak velocity residuals in azimuth (left column) and radial distance (right) in the ^{12}CO disk of HD 163296, obtained from analyses of the upper surface alone (top row) and of the combined contribution of upper and lower surfaces (bottom). Using this kinematical information, the clustering algorithm introduced in Section 3.4 detects two localized perturbations, P94 (top) and P261 (bottom), possibly associated with the presence of two giant planets in the disk. Blue circles are residuals extracted from 60 au wide radial sectors, centered at 86 (top) and 260 au (bottom). Error bars are computed according to the analytical treatment of uncertainties presented in Appendix A. The global peaks shown as black lines mark the median location of peak velocity residuals above 3σ significance with respect to the background velocities, which nearly follow a normal distribution as displayed in the rightmost subpanels. Note that outliers in the normal distributions are related to the localized perturbations. The mean value of all peak velocity residuals is 0.16 and 0.18 km s^{-1} for the P94 and P261 analyses, respectively, while 1σ equals 0.05 and 0.06 km s^{-1}, which represents the standard deviation of velocity residuals weighted by their uncertainties.

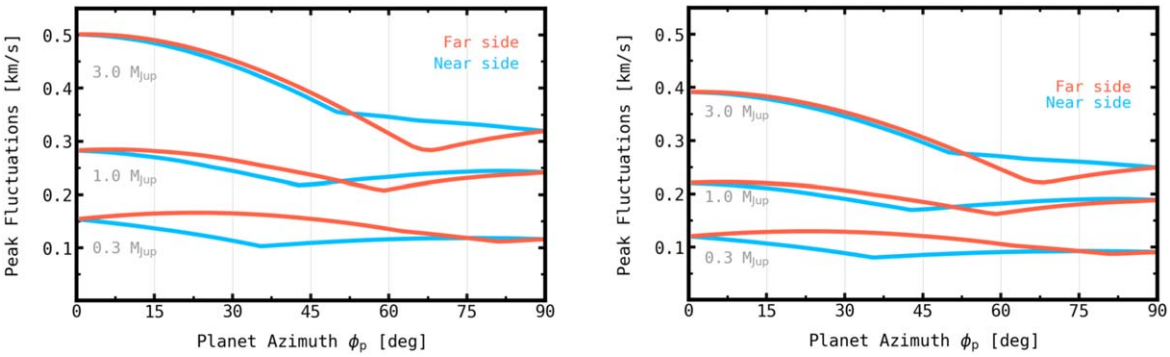

Figure 14. Simulated intrinsic peak velocity fluctuations as a function of planet azimuth, projected along a line of sight parallel to the minor axis of the disk, with an inclination of 45°. No radiative transfer effects are considered. These simulations are rescaled versions of those presented in Paper I, assuming a stellar mass of 2 $M_\odot$ and three different planet masses at a radius of $R = 94$ au (left) and $R = 141$ au (right). The P94 perturbation detected in this work at $R = 94$ au, $\phi = 50°$ on the near side of the disk is consistent with a $\sim$1 M_{Jup} planet, whose perturbation is expected to be amplified in folded residual maps owing to radiative transfer and projection effects as discussed in Section 3.4.1. The nondetection reported around the D141 gap suggests that an embedded planet at such an orbital radius, if any, should be less massive than half a Jupiter so that its kinematical perturbations go unnoticed with respect to the background fluctuations.

ORCID iDs

Andrés F. Izquierdo https://orcid.org/0000-0001-8446-3026
Stefano Facchini https://orcid.org/0000-0003-4689-2684
Giovanni P. Rosotti https://orcid.org/0000-0003-4853-5736
Ewine F. van Dishoeck https://orcid.org/0000-0001-7591-1907
Leonardo Testi https://orcid.org/0000-0003-1859-3070

References

Andrews, S. M. 2020, ARA&A, 58, 483
Andrews, S. M., Huang, J., Pérez, L. M., et al. 2018, ApJL, 869, L41
Bae, J., Teague, R., & Zhu, Z. 2021, ApJ, 912, 56
Bae, J., Zhu, Z., & Hartmann, L. 2017, ApJ, 850, 201
Bailer-Jones, C. A. L., Rybizki, J., Fouesneau, M., Mantelet, G., & Andrae, R. 2018, AJ, 156, 58
Bollati, F., Lodato, G., Price, D. J., & Pinte, C. 2021, MNRAS, 504, 5444
Casassus, S., & Pérez, S. 2019, ApJL, 883, L41
Disk Dynamics Collaboration, Armitage, P. J., Bae, J., et al. 2020, arXiv:2009.04345
Dong, R., Liu, S.-Y., & Fung, J. 2019, ApJ, 870, 72
Dullemond, C. P., Isella, A., Andrews, S. M., Skobleva, I., & Dzyurkevich, N. 2020, A&A, 633, A137
Flaherty, K. M., Hughes, A. M., Rose, S. C., et al. 2017, ApJ, 843, 150
Flaherty, K. M., Hughes, A. M., Rosenfeld, K. A., et al. 2015, ApJ, 813, 99
Foreman-Mackey, D., Hogg, D. W., Lang, D., & Goodman, J. 2013, PASP, 125, 306
Grady, C. A., Devine, D., Woodgate, B., et al. 2000, ApJ, 544, 895
Hacar, A., Alves, J., Burkert, A., & Goldsmith, P. 2016, A&A, 591, A104
Haffert, S. Y., Bohn, A. J., de Boer, J., et al. 2019, NatAs, 3, 749
Hunter, J. D. 2007, CSE, 9, 90
Isella, A., Guidi, G., Testi, L., et al. 2016, PhRvL, 117, 251101
Isella, A., Huang, J., Andrews, S. M., et al. 2018, ApJL, 869, L49
Izquierdo, A. F., Testi, L., Facchini, S., Rosotti, G. P., & van Dishoeck, E. F. 2021, A&A, 650, A179
Kanagawa, K. D., Tanaka, H., Muto, T., Tanigawa, T., & Takeuchi, T. 2015, MNRAS, 448, 994
Keppler, M., Benisty, M., Müller, A., et al. 2018, A&A, 617, A44
Koch, E. W., & Rosolowsky, E. W. 2015, MNRAS, 452, 3435
Liu, S.-F., Jin, S., Li, S., Isella, A., & Li, H. 2018, ApJ, 857, 87
MacQueen, J. 1967, in Proc. 5th Berkeley Symp. Math. Stat. Probab. 1, ed. L. M. Le Cam & J. Neyman (Oakland, CA: Univ. California Press), 281
Miotello, A., Bruderer, S., & van Dishoeck, E. F. 2014, A&A, 572, A96
Öberg, K. I., Guzmán, V. V., Walsh, C., et al. 2021, ApJS, 257, 1
Pedregosa, F., Varoquaux, G., Gramfort, A., et al. 2011, J. Mach. Learn. Res, 12, 2825, https://www.jmlr.org/papers/v12/pedregosa11a.html
Pérez, S., Casassus, S., & Benítez-Llambay, P. 2018, MNRAS, 480, L12
Perez, S., Dunhill, A., Casassus, S., et al. 2015, ApJL, 811, L5
Pinte, C., Ménard, F., Duchêne, G., et al. 2018a, A&A, 609, A47
Pinte, C., Price, D. J., Ménard, F., et al. 2018b, ApJL, 860, L13
Pinte, C., Price, D. J., Ménard, F., et al. 2020, ApJL, 890, L9
Pinte, C., van der Plas, G., Ménard, F., et al. 2019, NatAs, 3, 1109
Rabago, I., & Zhu, Z. 2021, MNRAS, 502, 5325
Rosenfeld, K. A., Andrews, S. M., Hughes, A. M., Wilner, D. J., & Qi, C. 2013, ApJ, 774, 16
Rosotti, G. P., Teague, R., Dullemond, C., Booth, R. A., & Clarke, C. J. 2020, MNRAS, 495, 173
Teague, R., Bae, J., Aikawa, Y., et al. 2021a, ApJS, 257, 18
Teague, R., Bae, J., & Bergin, E. A. 2019, Natur, 574, 378
Teague, R., Bae, J., Bergin, E. A., Birnstiel, T., & Foreman-Mackey, D. 2018, ApJL, 860, L12
Teague, R., & Foreman-Mackey, D. 2018, RNAAS, 2, 173
Teague, R., Law, C., Huang, J., & Meng, F. 2021b, JOSS, 6, 3827
Weaver, E., Isella, A., & Boehler, Y. 2018, ApJ, 853, 113
Woitke, P., Min, M., Pinte, C., et al. 2016, A&A, 586, A103
Zhang, S., Zhu, Z., Huang, J., et al. 2018, ApJL, 869, L47